Nano Research
2024, 17(4): 2360–2367
ISSN 1998-0124 CN 11-5974/O4
https://doi.org/10.1007/s12274-023-6068-1

High-throughput screening of single-atom catalysts confined in monolayer black phosphorus for efficient nitrogen reduction reaction

Xiao-Yan Li[1,§], Manyi Duan[2,§], and Pengfei Ou[1,3] (✉)

[1] Department of Electrical and Computer Engineering, University of Toronto, Toronto, Ontario M5S 1A4, Canada
[2] School of Physics and Electronic Engineering, Sichuan Normal University, Chengdu 610101, China
[3] Department of Chemistry, Northwestern University, Evanston, IL 60208, USA
[§] Xiao-Yan Li and Manyi Duan contributed equally to this work.

Received: 31 May 2023 / **Revised:** 22 July 2023 / **Accepted:** 7 August 2023

ABSTRACT

The discovery of metal-nitrogen centers as the active sites for electrolysis has aroused significant interest in utilizing single-atom catalysts for nitrogen reduction reaction (NRR). Properly designed nanostructured catalysts that strongly interact with nitrogen molecules (N_2) can promote adsorption and activation, thereby resulting in efficient catalysts with high stability, activity, and selectivity. In this study, using density functional theory calculations, we selected monolayer black phosphorus (BP) as the substrate and screened a series of single-atom transition metals confined in tri-coordinated and tetra-coordinated active centers (without and with N dopants) to electro-catalyze NRR. As a result, we have identified two promising candidates (Hf_1-N_1P_2-1 and Tc_1-N_4), which exhibit not only low overpotentials of 0.56 and 0.49 V but also high thermodynamic and electrochemical stability, as well as good selectivity towards NRR over the competing hydrogen evolution reaction. We also demonstrate the ability of Hf_1-N_1P_2-1 and Tc_1-N_4 to activate and hydrogenate N_2 by donating electrons and regulating charge transfer. This study not only predicts new BP-based promising catalysts but also provides guidance for the rational design of high-performance NRR electrocatalysts under ambient conditions.

KEYWORDS

N_2 electroreduction reaction, single-atom catalysts, black phosphorus, density functional theory, high-throughput calculations

1 Introduction

Electrocatalytic conversion of nitrogen (N_2) to ammonia has garnered significant interest and has far-reaching ramifications for scientific study [1–3], as it uses significantly less energy and generates less environmental pollution than the conventional Haber–Bosch process that occurs at extremely high temperatures and pressures [4, 5]. As an inert gas, N_2 makes up 78.1% of the earth's atmosphere, has a high bond energy (940.95 kJ·mol^{-1}), low electron affinity (–1.9 eV), and high ionization energy (15.85 eV), which cause a huge challenge to break the strong N≡N triple bond under ambient conditions [6]. The reaction rate of high-productivity ammonia synthesis is still greatly limited despite decades of extensive research into potential catalysts [7–9]. Electrocatalytic nitrogen reduction reaction (NRR) occurs under an appropriate external voltage, but with its relatively high equilibrium potentials, NRR will, unfortunately, compete with the hydrogen evolution reaction (HER) in acidic/alkaline solutions [10–12]. In addition, this complex NRR involves multiple proton/electron transfers and the adsorption of various intermediates, which are not conducive to the occurrence of ammonia synthesis. Therefore, one of the effective methods to improve the NRR activity and selectivity is the rational design of catalysts loaded with highly active sites for N_2 adsorption and activation, as well as HER inhibition.

The productivity of ammonia in NRR is highly dependent on the physicochemical characteristics of the catalyst, such as electronic and surface structure [13, 14]. Currently, two-dimensional (2D) materials (e.g., graphene, MoS_2, and MXenes) are utilized for NRR and have been generally reported to possess catalytic activity for ammonia [9, 15–18]. Nonetheless, the active sites for most 2D materials are concentrated at the edges, and the majority of surfaces are catalytically inactive, restricting ammonia synthesis. It is noteworthy that single-atoms-anchored N-doped carbon materials have been demonstrated to be beneficial for NRR due to the high inherent catalytic activity in these novel metal-nitrogen active sites [19–21]. For instance, anchoring the single-atom Ru onto N-doped carbon has resulted in a high Faradaic efficiency (FE) of 29.6% at –0.2 V vs. reversible hydrogen electrode (RHE) [22]. Therefore, applying defect engineering techniques such as vacancies, single-atom doping of transition metals (TMs), and non-metallic atom doping, is an instructive strategy for modifying the electronic structure, electron transfer, and intermediate adsorption on the surface of single-atom catalyst (SAC) [23, 24].

Recently, well-exfoliated few-layer black phosphorus (BP) was

Address correspondence to pengfei.ou@northwestern.edu

reported as a promising catalyst for NRR with a high ammonia yield of 31.37 μg·h^{-1}·mg$_{cat}^{-1}$ [25]. Previous theoretical studies also suggested that SACs anchored on BP (e.g., B-SAC and Mo-SAC) could be potential metal-free electrocatalysts for NRR [26–29]. This inspired us to screen for more promising single-atom electrocatalysts based on TMs confined in various defect/doping BP surfaces. In this work, we used the high-throughput density functional theory (DFT) calculations and proposed two promising electrocatalysts of Hf_1-N_1P_2-1 and Tc_1-N_4, which exhibit low overpotentials of 0.56 and 0.49 V, respectively, where the potential-limiting step (PLS) is *N–N to *N–NH. The electronic structure calculations indicate that Hf_1-N_1P_2-1 and Tc_1-N_4 sites are good electron donors for the activation and hydrogenation of N_2. Our study suggests that Hf_1-N_1P_2-1 and Tc_1-N_4 are promising catalysts for NRR over the competing HER process, which provides a new impetus for electrocatalytic efficient NRR.

2 Computational details

All spin-polarized DFT calculations were performed by employing the projector-augmented wave (PAW) method as implemented in the Vienna *ab initio* simulation package (VASP) [30–32]. The generalized gradient approximation in the parametrization of Perdew–Burke–Ernzerhof (GGA-PBE) was implemented to describe the exchange-correlation function [33, 34]. A plane-wave cut-off of 450 eV was adopted for a plane-wave basis set. The *k*-point in the Brillouin zone was sampled with a 2 × 2 × 1 grid generated by the Monkhorst–Pack scheme [35]. A vacuum region of about 20 Å thickness was included along the perpendicular direction to avoid artificial interactions. The self-consistent convergence criteria of energy and force were set to less than 10^{-5} eV and 0.01 eV·Å^{-1}. For the non-self-consistent electronic structure calculations, the *k*-point in the Brillouin zone and energy convergence were increased to 4 × 4 × 1 grid and 10^{-6} eV, respectively. The transferred charge was computed by Bader charge analysis [36]. The *ab initio* molecular dynamics (AIMD) simulations were conducted to directly evaluate the thermodynamic stability of catalyst structure in the canonical ensemble (NVT) with Nosé–Hoover thermostat at room temperature (300 K) for a time period of 20 ps [37, 38].

In NRR, the reaction energy (ΔG) for each elementary step was obtained using the computational hydrogenation electrode (CHE) model proposed by Nørskov et al. [39], which equation is shown below

$$\Delta G = \Delta E + \Delta E_{\mathrm{ZPE}} - T\Delta S + neU + \Delta G_{\mathrm{pH}} \tag{1}$$

where ΔE refers to the electronic energy difference from the DFT calculations, ΔE_{ZPE} and ΔS are the changes in zero-point energy and entropy, respectively. The temperature T is set to be room temperature of 300 K. n and U are the number of electrons transferred and the applied potential. ΔG_{pH} is the free energy correction from pH in the solvation environment. Here, we assume pH = 0, so it results in $\Delta G_{\mathrm{pH}} = 0$ eV. The energy of a nitrogen and hydrogen atom in a N_2 and H_2 molecule in its gas phase was used as the reference state of N and H.

For the single atom, its binding energy (E_b) in SAC and its metal cohesive energy (E_{coh}) in the bulk form are calculated by the following two equations

$$E_{\mathrm{b}} = E_{\mathrm{M_1-N_xP_y}} - E_{\mathrm{M_{single}}} - E_{\mathrm{N_xP_y}} \tag{2}$$

$$E_{\mathrm{coh}} = (E_{\mathrm{M_{bulk}}})/N - E_{\mathrm{M_{single}}} \tag{3}$$

where $E_{\mathrm{M_{bulk}}}$, $E_{\mathrm{M_{single}}}$, $E_{\mathrm{M_1-N_xP_y}}$, $E_{\mathrm{N_xP_y}}$, and N refer to the bulk energy of transition metal in the united cell, the energy of a single atom in a vacuum, the total energy of SAC, the total energy of the substrate, and the number of atoms in the unit cell, respectively.

According to the CHE model [40], the overpotential (η) for NRR is determined by the lowest applied potential to drive the PLS with the most positive ΔG ($\Delta G_{\max}$) to proceed, as computed by

$$\eta = U_{\mathrm{equilibrium}} - U_{\mathrm{limiting}} \tag{4}$$

where $U_{\mathrm{equilibrium}}$ is the equilibrium potential for NRR and U_{limiting} is the applied potential to eliminate the reaction energy of the PLS. The value of U_{limiting} is calculated by

$$U_{\mathrm{limiting}} = -\Delta G_{\max}/e \tag{5}$$

where η serves as a good indicator for catalytic activity, i.e., a smaller value of η indicates an easier NRR process.

3 Results and discussion

We began by developing a high-throughput screening strategy [41–44] (Scheme 1) that integrates the Scheme 1(1) generation of all possible atomic configurations, the evaluation of Scheme 1(2) thermodynamic and electrochemical stability, Scheme 1(3) activity and selectivity, and Scheme 1(4) mechanism analysis including the reaction pathways, partial density of states (PDOS), charge density difference, and Bader charge analysis.

3.1 Structural stability of SACs in electrochemistry

Despite the outstanding electrocatalytic activity of SACs, the practical application of these catalysts heavily relies on their long-term stability and durability. To account for the structural stability, we conducted a thorough design and optimization of SACs geometries onto BP substrates. We explored 16 coordination environments of SACs anchored on the pristine BP and N-doped BP substrates (a 5 × 3 supercell with a dimension of 13.17 Å × 13.32 Å) by varying the ratio between N and P (x and y), the element type of TMs (M), and three-fold and four-fold coordination constructed from single-P-vacancy and double-P-vacancy defects (Fig. S1 in the Electronic Supplementary Material (ESM)) in M-N_xP_y-n centers, as shown in Fig. 1. Using DFT calculations, we investigated the thermodynamic and electrochemical stabilities of 3d-, 4d-, and 5d-TM SACs, resulting in a total of ~ 464 SACs (16 × 29) with combinations between coordination environments and TMs.

We calculated the stability energy ($E_{\mathrm{stability}}$) of 464 SACs and summarized the results in Fig. S2 in the ESM to evaluate the thermodynamic stability of SACs. The $E_{\mathrm{stability}}$ is defined as below [13]

$$E_{\mathrm{stability}} = E_{\mathrm{b}} - E_{\mathrm{coh}} \tag{6}$$

where E_b and E_{coh} are the binding energy of SAC and metal cohesive energy in its bulk form, respectively. A negative value of $E_{\mathrm{stability}}$ signifies a preference for the TM atom to form a single-atom center rather than aggregate into metal clusters. The calculated values of $E_{\mathrm{stability}}$ in Fig. S2 in the ESM reveal that early TMs, particularly 3d-Sc, 4d-Y, 4d-Zr, and 5d-Hf, exhibit strong thermodynamic affinity for interacting with the substrates with 16 different types of coordination environments considered. In contrast, the formation of SACs on BP substrate from 4d-Mo, -Tc, and -Ru, as well as 5d-W, -Re, and -Os, is predicted to be less favorable based on the analysis of thermodynamic stability.

Meanwhile, the electrochemical stability was estimated in terms of the dissolution potential (U_{diss})

$$U_{\mathrm{diss}} = U^0_{\mathrm{diss}}\,(\mathrm{metal, bulk}) - E_{\mathrm{stability}}/ne \tag{7}$$

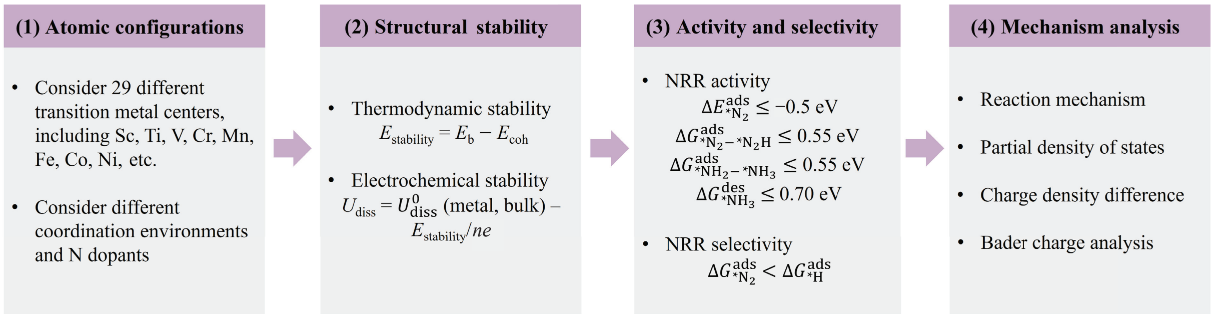

Scheme 1 High-throughput screening of SACs confined in BP substrates for NRR.

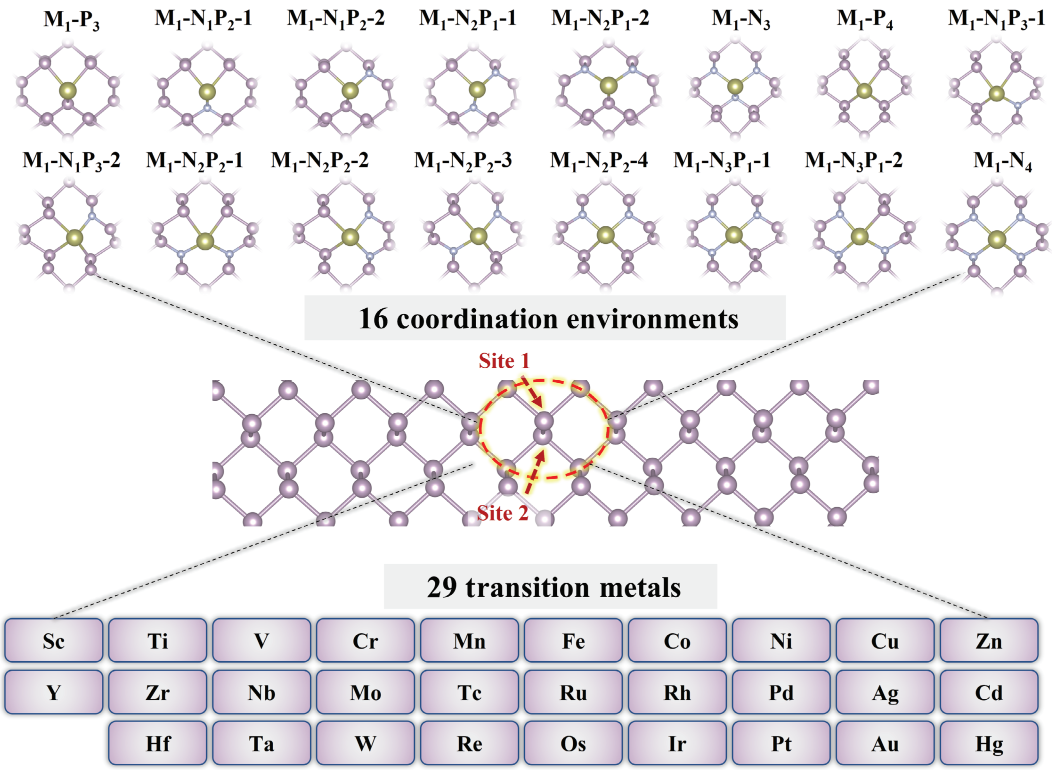

Figure 1 The SACs with three-fold and four-fold coordinations anchored in BP-based substrate for NRR. Here, 16 coordination environments traversed 29 transition metals, respectively. Phosphorus, purple; nitrogen, grey; and transition metals, gold.

where U^0_{diss}(metal, bulk) and n are the standard dissolution potential of bulk metal and the number of electrons involved in the dissolution [44], respectively. Positive U_{diss} values indicate these catalysts are electrochemically stable and less likely to dissolve under acidic conditions. The pioneering works claim the reliability and feasibility of this approach, as the majority of the experimentally synthesized SACs demonstrate both thermodynamical and electronic stability according to these evaluation criteria [43–45]. Figure S3 in the ESM summarizes the U_{diss} values of ~ 464 SACs, which displays that certain late 3d-, 4d-, and 5d-TMs can maintain high stabilities of SACs in the electrochemical environment, such as Ru, Rh, Pd, Ag, and Cd in 4d-TMs, as well as Os, Ir, Pt, and Au in 5d-TMs. In addition, we also found that some early 5d-TMs, including Hf, Ta, W, and Re, exhibit insolubility and retain a stable single-atom configuration in the electrochemical environment.

Combining $E_{stability}$ and U_{diss} (all original results are provided in Supplementary Data 1 in the ESM), Fig. 2 classifies ~ 464 SAC systems into four groups using stability evaluation criteria from the previous study [41]. Although almost all 3d-TMs showcase the tendency to form stable single-atom configurations on different BP surfaces, only a few late 3d-TMs, such as Co, Ni, and Cu, were found to exhibit additional stability in solution environments of electrocatalysis. Among 4d- and 5d-TMs, Ru, Rh, Pd, Ag, Cd, Hf, Ir, Pt, and Au also display superior thermodynamic and electrochemical stabilities in most coordination environments studied here. Overall, 188 SACs colored purple in Fig. 2 have been identified as systems with high structural stability and insolubility, indicating their excellent stability during the electrocatalytic reactions.

3.2 Activity and selectivity of SACs in NRR

Following the structural stability screening of SACs, we calculated the adsorption energy of N_2 ($\Delta E^{ads}_{*N_2}$) in end-on and side-on configurations, as shown in Fig. S4 in the ESM. Our results indicate that N_2 molecules prefer to be adsorbed on the surfaces of these SACs via the end-on configuration. We also found that the adsorption energy of N_2 is dependent on the number of d electrons of TMs, where early TM-SACs show a stronger binding strength with the N_2 molecule compared to their late TM counterparts. For example, the adsorption energy of Co in 3d-TMs is more negative than Zn, Ru is more negative than Cd in 4d-TMs, and Hf is more negative than Au in 5d-TMs, indicating the more favorable N_2 adsorption and activation on those early TM-SACs. This can be explained by the bonding characteristics between TMs and N_2 molecules, where the d electrons of early TM atoms are more likely to be donated to N_2 than the late TM metals, as illustrated in Fig. S5 in the ESM, where Ru transfers

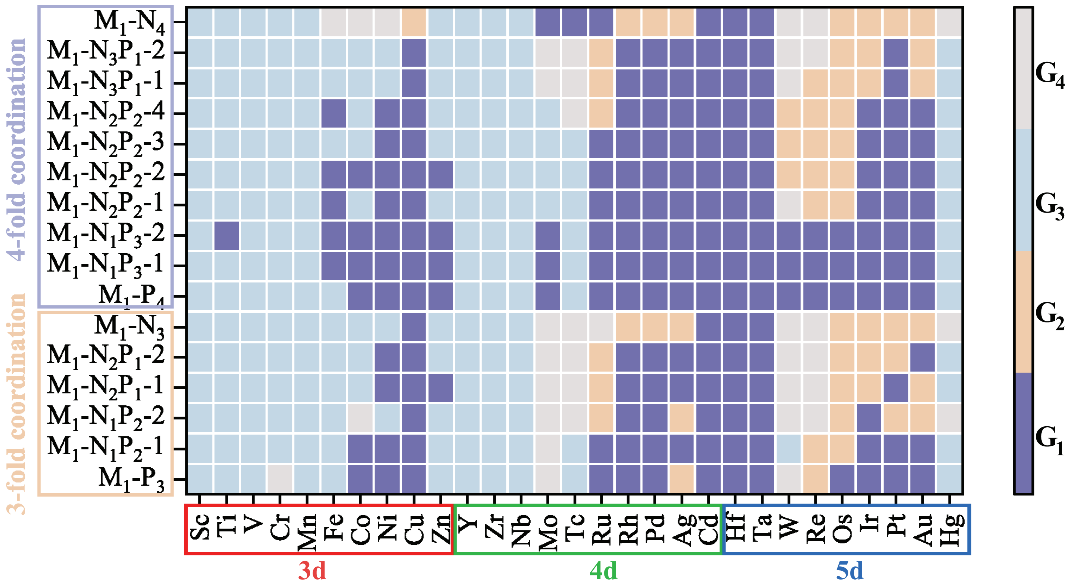

Figure 2 Stability classification of SACs represented by various colors. G_1: unaggregatable and indissoluble, G_2: aggregatable and indissoluble, G_3: unaggregatable and dissoluble, and G_4: aggregatable and dissoluble.

more electrons to the adsorbed N_2 relative to Cd, resulting in a stronger binding strength with N_2.

We then computed the reaction energy of $*N_2$ protonation ($\Delta G^{rnx}_{*N_2-*N_2H}$) based on the end-on configuration of $*N_2$. To assess the catalytic activity in NRR, we used screening criteria from pioneering studies, where the adsorption energy of N_2 on the catalyst surface should be lower than −0.5 eV ($\Delta E^{ads}_{*N_2} \leq -0.5$ eV) and the reaction energy of $*N_2$ hydrogenation should be less than 0.55 eV ($\Delta G^{rnx}_{*N_2-*N_2H} \leq 0.55$ eV) [46, 47]. Using these criteria, we identified some SACs that exhibit a smaller limiting potential than those of the best pure TM catalysts predicted previously [48]. As shown in Fig. 3(a), we divided the figure into four distinct regions: The upper-right region represents the catalysts that do not convert $*N_2$ into $*N_2H$; the lower-right region means catalysts that can reduce $*N_2$ into $*N_2H$ but cannot capture N_2; the upper-left region corresponds to the candidates with a strong binding strength to N_2 but low performance for its reduction; and only the lower-left region where the catalysts are marked by green solid circles satisfy both the criteria we have set. We observed that most catalyst systems are filtered out, leaving only 21 potential SACs for our next-step screening of ammonia generation.

We applied additional criteria of reaction energy of $*NH_2$ protonation and desorption energy of *NH3 ($\Delta G^{rnx}_{*NH_2-*NH_3} \leq$ 0.55 eV and $\Delta G^{des}_{*NH_3} \leq 0.70$ eV) [46, 47] to evaluate the onset potential and assess the rate of ammonia generation in NRR. Our calculated results were divided into four categories, which are shown in Fig. 3(b). Materials located in the upper-right region fail to meet both criteria. The upper-left and lower-right regions hold the materials that only satisfy one criterion, whereas only the lower-left region contains materials that fulfill both criteria. Nine SAC systems (Ta_1-N_1P_2-2, Hf_1-N_1P_2-1, W_1-P_4, Re_1-N_1P_3-1, W_1-N_1P_3-1, Re_1-N_1P_3-1, W_1-N_1P_3-2, Re_1-N_1P_3-2, and Tc_1-N_4) were finally screened out as promising candidates for highly active catalysts for NRR. Among these candidates, the number of SACs with four-fold coordination is much larger than that with three-fold coordination (7 vs. 2). This can be attributed to the unique structural characteristic of BP, which causes the strong interaction between the TM d-electrons with the four-fold coordination environment, enabling the TM d-orbitals that can interact more strongly with the reaction intermediates of NRR.

Considering the selectivity between NRR and its competing HER, we compared the adsorption free energies of $*N_2$ and *H on the surfaces of screened 9 SACs [49]. These results are illustrated in Fig. 3(c), where the catalysts in the upper-left corner and lower-right corner are the adsorption dominants of *H and $*N_2$, respectively. We find that only 3 candidates, i.e., Hf_1-N_1P_2-1, Ta_1-N_1P_2-2, and Tc_1-N_4 (Fig. 3(d)), show the preference for $*N_2$ adsorption relative to *H adsorption, indicating a high selectivity of NRR over HER.

3.3 Reaction mechanism of NRR of the screened catalyst

We considered the alternating and distal pathways (Fig. S6 in the ESM) and summarized the energetics of elementary steps in NRR on the surfaces of three screened catalysts in Fig. 4 and Fig. S7 in the ESM, where the corresponding atomic configurations of DFT-optimized intermediates on the catalyst surfaces are shown in Fig. S8 in the ESM. The free energies of N_2 adsorption on Hf_1-N_1P_2-1, Tc_1-N_4, and Ta_1-N_1P_2-2 are −0.09, −0.11, and −0.51 eV via the end-on configuration, respectively. The onset potentials of NRR on the surfaces of Hf_1-N_1P_2-1 and Tc_1-N_4 are −0.56 (Figs. 4(a) and 4(b)) and −0.49 V (Figs. 4(d) and 4(e)), where the PLSs both are *N–N to *N–NH along the alternating and distal pathways. However, Ta_1-N_1P_2-2 shows other PLSs along different pathways (Fig. S7 in the ESM), where PLSs of Ta_1-N_1P_2-2 are the step of *NH–NH_2 to *NH_2–NH_2 with the onset potential of −0.82 V and the step of *NH–NH to *NH–NH_2 with the onset potential of −1.13 V along the alternating and distal pathways, respectively. Therefore, we conducted additional AIMD simulations to evaluate the thermodynamic stability of Hf_1-N_1P_2-1 and Tc_1-N_4 at 300 K. After simulating for 20 ps, we noticed negligible changes in the final structures (insets in Figs. 4(c) and 4(f)) compared to the initial structures (Fig. 3(d)), and temperatures fluctuate dynamically around 300 K (Fig. S9 in the ESM), indicating their good structural stability at room temperature. In general, Hf_1-N_1P_2-1 and Tc_1-N_4 are relatively promising catalysts, where the adsorption and hydrogenation of N_2 determine the activity and selectivity of NRR.

Therefore, we investigated the electronic structures of Hf_1-N_1P_2-1 and Tc_1-N_4 to elucidate the reason behind the outstanding performance of the single atoms Hf- and Tc-anchored BP for NRR. Figures 5(a) and 5(d) show the PDOSs of Hf_1-N_1P_2-1 and Tc_1-N_4 before N_2 adsorption. We find that PDOSs of Hf (5d) and Tc (4d) are spin-polarized asymmetric and show that d orbitals of Hf and Tc hybridized with p orbitals of P or N atoms in the substrate (Figs. S10 and S12 in the ESM). After adsorbing N_2, the overlapped PDOS between Hf (5d) and $*N_2$ (2p) is observed in

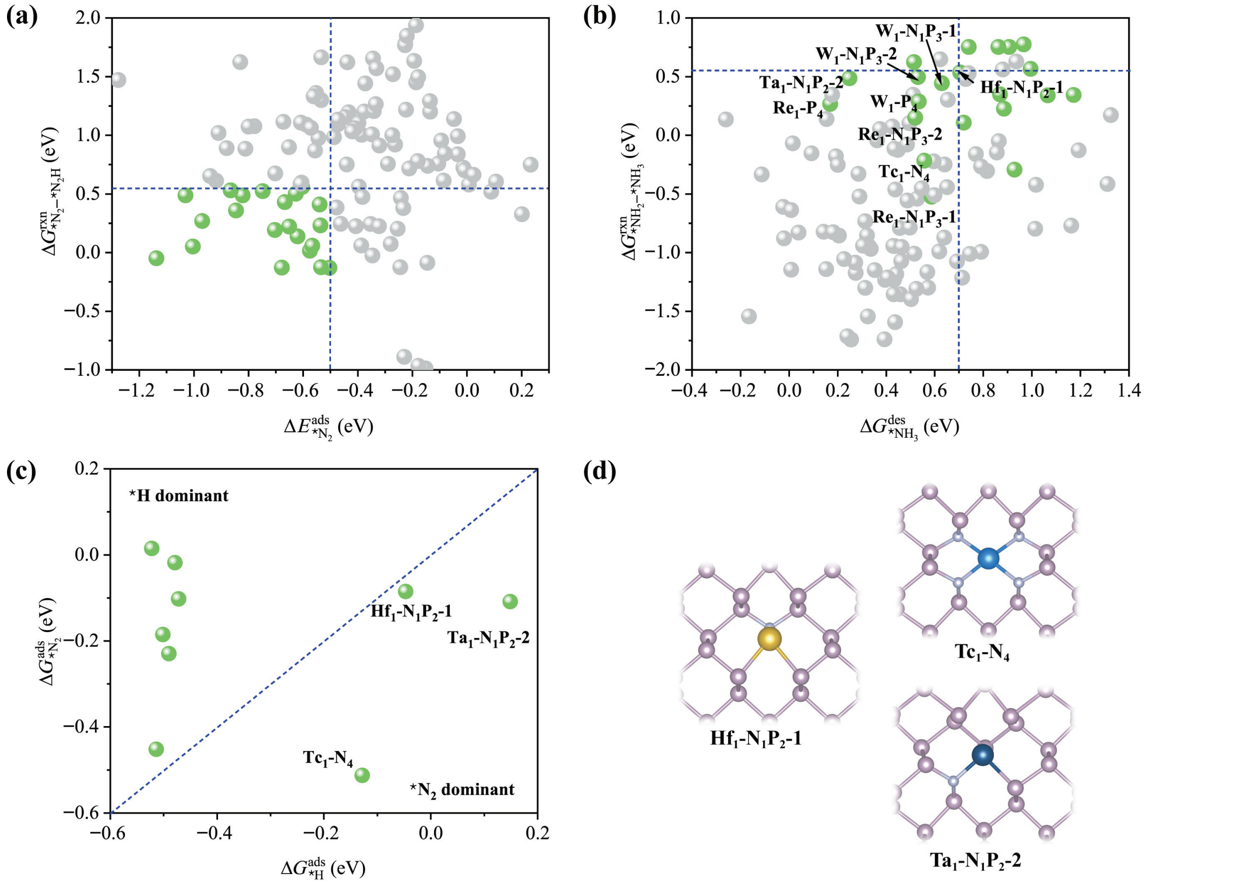

Figure 3 (a) First-step screening of SACs for NRR based on their performance for N_2 adsorption and $^*N_2$ protonation into $^*N_2H$. (b) Second-step screening of SACs for NRR based on their performance for $^*NH_3$ generation from $^*NH_2$ and its desorption. (c) Computed free energies for *H and $^*N_2$ adsorption on SACs. (d) Geometries of Hf_1-N_1P_2-1, Tc_1-N_4, and Ta_1-N_1P_2-2. Phosphorus, purple; nitrogen, grey; hafnium, yellow; tantalum, indigo; and technetium, blue.

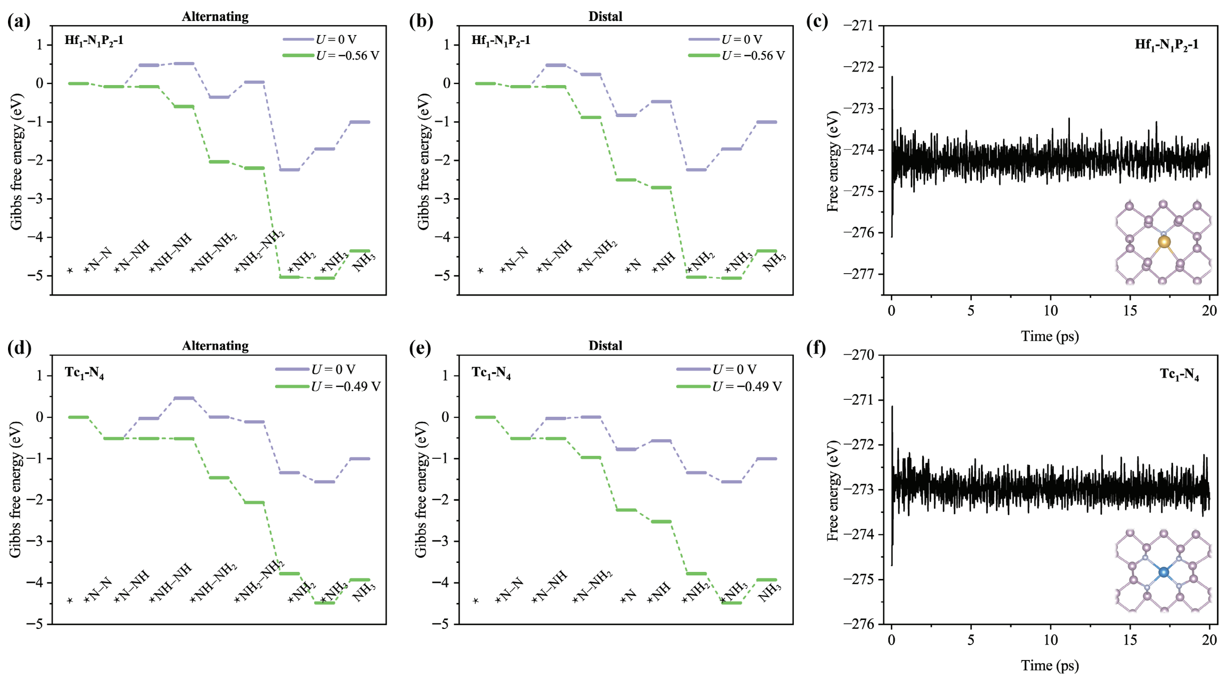

Figure 4 (a) and (b) Free-energy diagrams of NRR on Hf_1-N_1P_2-1 along the alternating and distal pathways. (c) Free energy of AIMD simulation for 20 ps on Hf_1-N_1P_2-1 at 300 K. (d) and (e) Free-energy diagrams of NRR on Tc_1-N_4 along the alternating and distal pathways. The purple and green curves correspond to the free energy changes for NRR at 0 V and onset potentials vs. RHE, respectively. (f) Free energy profile of AIMD simulation for 20 ps on Tc_1-N_4 at 300 K. The insert configurations are the structures at 20 ps in AIMD simulations. Phosphorus, purple; nitrogen, grey; hafnium, yellow; and technetium, blue.

Fig. 5(b). These overlapped PDOSs are mainly contributed by the couplings of Hf $(d_{yz}, d_{xz}, d_{x^2-y^2})$–$^*N_2$ (p_x, p_y) (Fig. S11 in the ESM). For Tc_1-N_4 in Fig. 5(e), the interaction between the N_2 molecule and substrate is described by the overlapped PDOS between Tc (4d) and $^*N_2$ (2p) that origins from the couplings of Tc $(d_{xz}, d_{x^2-y^2})$–$^*N_2$ (p_x, p_y) and Tc (d_{xy}, d_{yz}, d_{xz})–$^*N_2$ (p_x, p_y, p_z) (Fig. S13 in the ESM). We further plotted the charge density difference that shows electron transfers from Hf (Tc) to the adsorbed N_2 in

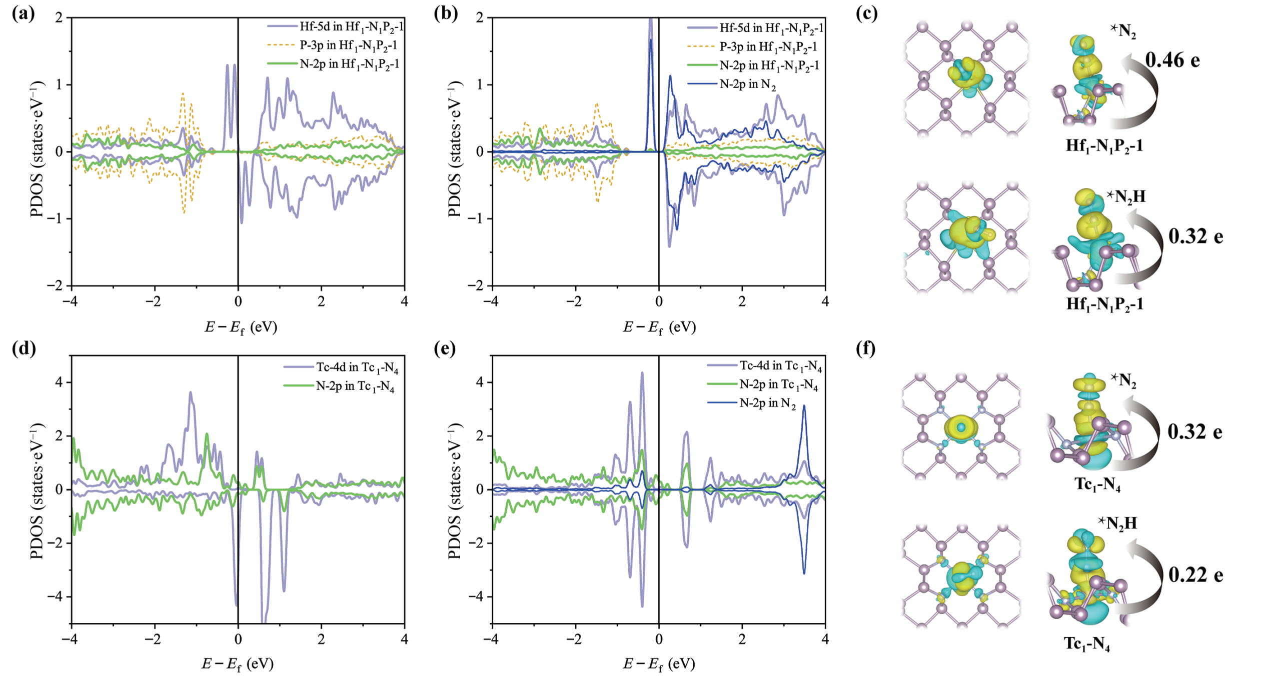

Figure 5 (a) and (b) PDOSs of Hf-5d, P-3p, and N-2p before and after N_2 adsorption. (c) The charge density difference between the Hf_1-N_1P_2-1 and adsorbates of *N_2 and *N_2H with the isosurface value of 0.002 e·Bohr^{-3}. (d) and (e) PDOSs of Tc-4d and N-2p before and after N_2 adsorption. (f) The charge density difference between the Tc_1-N_4 and adsorbates of *N_2 and *N_2H with the isosurface value of 0.002 e·Bohr^{-3}.

Fig. 5(c) (Fig. 5(f)), resulting in the stretched N–N bond length with 1.14 Å (1.14 Å) basis of free N_2 molecule with 1.10 Å. The Bader charge analysis [36] also confirmed that 0.46 e (0.32 e) were accumulated on the *N_2 adsorbate on Hf_1-N_1P_2-1 (Tc_1-N_4), suggesting the Hf_1-N_1P_2-1 (Tc_1-N_4) sites can activate the N_2 molecule by donating electrons. Following the succeeding *N_2 protonation steps, we plotted the charge density difference of *NH_2 adsorbate on Tc_1-N_4 and analyzed the Bader charge transfer in Fig. 5(d), where Hf_1-N_1P_2-1 (Tc_1-N_4) transfers 0.32 e (0.22 e) to *NH_2 adsorbate. We observe that the accumulated electrons on Hf_1-N_1P_2-1 and Tc_1-N_4 contribute to the activation and subsequent protonation of adsorbed *N_2, therefore, resulting in the best-performance electrocatalyst for NRR with the lowest limiting potentials among the screened candidates. Generally, the N_2 adsorption is enhanced with higher N doping ratios in Hf_1-N_xP_y ($x + y = 3$) and Tc_1-N_xP_y ($x + y = 4$) sites, as evident from our analysis of the N doping effect on Bader charge (Fig. S14 in the ESM). We note that the radioactivity of Tc should be delicately addressed during the experimental validation of Tc_1-N_4.

4 Conclusions

In summary, we have systematically examined the candidacy of 3d-, 4d-, and 5d-SACs confined in BP substrates for efficient electrochemical NRR. Using high-throughput DFT calculations, we revealed that Hf_1-N_1P_2-1 and Tc_1-N_4 exhibit good thermodynamic and electrochemical stability, as well as high catalytic activity and selectivity for NRR. The preferred reaction mechanisms of the NRR are the alternating and distal pathways on the surfaces of Hf_1-N_1P_2-1 and Tc_1-N_4 due to the stable N_2 adsorption with end-on configuration. On Hf_1-N_1P_2-1 and Tc_1-N_4, the overpotentials of NRR are as low as 0.56 and 0.49 V, where the PLS is *N_2 to *N_2H. The calculated electronic structures of Hf_1-N_1P_2-1 and Tc_1-N_4 before and after the N_2 adsorption demonstrate the reaction site as the electron donor can activate and hydrogenate N_2 by donating electrons and regulating charge transfer to intermediates. Our results reveal the new single-atom catalysts of Hf_1-N_1P_2-1 and Tc_1-N_4 confined in BP exhibit intrinsic NRR activity and selectivity, which also provides guidance for the experimental synthesis of stable and efficient single-atom catalysts for electrochemical NRR.

Acknowledgements

We acknowledge the financial support from the National Natural Science Foundation of China (No. 11404230) and the Foundation of Science and Technology Bureau of Sichuan Province (No. 2013JY0085). We also acknowledge the Niagara supercomputer at the SciNet HPC Consortium. SciNet is funded by: the Canada Foundation for Innovation; the Government of Ontario; the Ontario Research Fund-Research Excellence; and the University of Toronto. The authors also acknowledge the computing resources from the High-Performance Computing Center of Sichuan Normal University.

Electronic Supplementary Material: Supplementary material (calculated stability energy, dissolution energy, adsorption energy of N_2, difference of charged density, PDOSs, and so on) is available in the online version of this article at https://doi.org/10.1007/s12274-023-6068-1.

References

[1] Fu, X. B.; Pedersen, J. B.; Zhou, Y. Y.; Saccoccio, M.; Li, S. F.; Sažinas, R.; Li, K.; Andersen, S. Z.; Xu, A. N.; Deissler, N. H. et al. Continuous-flow electrosynthesis of ammonia by nitrogen reduction and hydrogen oxidation. *Science* **2023**, *379*, 707–712.

[2] Li, K.; Andersen, S. Z.; Statt, M. J.; Saccoccio, M.; Bukas, V. J.; Krempl, K.; Sažinas, R.; Pedersen, J. B.; Shadravan, V.; Zhou, Y. Y. et al. Enhancement of lithium-mediated ammonia synthesis by addition of oxygen. *Science* **2021**, *374*, 1593–1597.

[3] MacLeod, K. C.; Holland, P. L. Recent developments in the homogeneous reduction of dinitrogen by molybdenum and iron. *Nat. Chem.* **2013**, *5*, 559–565.

[4] van der Ham, C. J. M.; Koper, M. T. M.; Hetterscheid, D. G. H. Challenges in reduction of dinitrogen by proton and electron transfer. *Chem. Soc. Rev.* **2014**, *43*, 5183–5191.

[5] Qing, G.; Ghazfar, R.; Jackowski, S. T.; Habibzadeh, F.; Ashtiani,

M. M.; Chen, C. P.; Smith III, M. R.; Hamann, T. W. Recent advances and challenges of electrocatalytic N_2 reduction to ammonia. *Chem. Rev.* **2020**, *120*, 5437–5516.
[6] Jia, H. P.; Quadrelli, E. A. Mechanistic aspects of dinitrogen cleavage and hydrogenation to produce ammonia in catalysis and organometallic chemistry: Relevance of metal hydride bonds and dihydrogen. *Chem. Soc. Rev.* **2014**, *43*, 547–564.
[7] Bao, D.; Zhang, Q.; Meng, F. L.; Zhong, H. X.; Shi, M. M.; Zhang, Y.; Yan, J. M.; Jiang, Q.; Zhang, X. B. Electrochemical reduction of N_2 under ambient conditions for artificial N_2 fixation and renewable energy storage using N_2/NH_3 cycle. *Adv. Mater.* **2017**, *29*, 1604799.
[8] Logadóttir, Á.; Nørskov, J. K. Ammonia synthesis over a Ru (0001) surface studied by density functional calculations. *J. Catal.* **2003**, *220*, 273–279.
[9] Zhang, L.; Ji, X. Q.; Ren, X.; Ma, Y. J.; Shi, X. F.; Tian, Z. Q.; Asiri, A. M.; Chen, L.; Tang, B.; Sun, X. P. Electrochemical ammonia synthesis via nitrogen reduction reaction on a MoS_2 catalyst: Theoretical and experimental studies. *Adv. Mater.* **2018**, *30*, 1800191.
[10] Choi, C.; Back, S.; Kim, N. Y.; Lim, J.; Kim, Y. H.; Jung, Y. Suppression of hydrogen evolution reaction in electrochemical N_2 reduction using single-atom catalysts: A computational guideline. *ACS Catal.* **2018**, *8*, 7517–7525.
[11] Zhang, Q.; Wang, X.; Zhang, F. C.; Fang, C. Y.; Liu, D.; Zhou, Q. J. A high-throughput screening toward efficient nitrogen fixation: Transition metal single-atom catalysts anchored on an emerging π–π conjugated graphitic carbon nitride (g-$C_{10}N_3$) substrate with Dirac dispersion. *ACS Appl. Mater. Interfaces* **2023**, *15*, 11812–11826.
[12] Yao, Y.; Zhu, S. Q.; Wang, H. J.; Li, H.; Shao, M. H. A spectroscopic study on the nitrogen electrochemical reduction reaction on gold and platinum surfaces. *J. Am. Chem. Soc.* **2018**, *140*, 1496–1501.
[13] Lin, X. Y.; Wang, Y. T.; Chang, X.; Zhen, S. Y.; Zhao, Z. J.; Gong, J. L. High-throughput screening of electrocatalysts for nitrogen reduction reactions accelerated by interpretable intrinsic descriptor. *Angew. Chem., Int. Ed.* **2023**, *62*, e202300122.
[14] Chen, S. Y.; Gao, Y. Q.; Wang, W. G.; Prezhdo, O. V.; Xu, L. Prediction of three-metal cluster catalysts on two-dimensional W_2N_3 support with integrated descriptors for electrocatalytic nitrogen reduction. *ACS Nano* **2023**, *17*, 1522–1532.
[15] Lei, F. C.; Xu, W. L.; Yu, J.; Li, K.; Xie, J. F.; Hao, P.; Cui, G. W.; Tang, B. Electrochemical synthesis of ammonia by nitrate reduction on indium incorporated in sulfur doped graphene. *Chem. Eng. J.* **2021**, *426*, 131317.
[16] Shen, P.; Li, X. C.; Luo, Y. J.; Guo, Y. L.; Zhao, X. L.; Chu, K. High-efficiency N_2 electroreduction enabled by Se-vacancy-rich WSe_{2-x} in water-in-salt electrolytes. *ACS Nano* **2022**, *16*, 7915–7925.
[17] Laishram, D.; Kumar, D.; Shejale, K. P.; Saini, B.; Harikrishna; Krishnapriya, R.; Sharma, R. K. 2D transition metal carbides (MXenes) for applications in electrocatalysis. In *Heterogeneous Nanocatalysis for Energy and Environmental Sustainability*. Sudarsanam, P.; Yamauchi, Y.; Bharali, P., Eds.; John Wiley & Sons Ltd.: Hoboken, 2022; pp 165–198.
[18] Yang, T.; Song, T. T.; Zhou, J.; Wang, S. J.; Chi, D. Z.; Shen, L.; Yang, M.; Feng, Y. P. High-throughput screening of transition metal single atom catalysts anchored on molybdenum disulfide for nitrogen fixation. *Nano Energy* **2020**, *68*, 104304.
[19] Liu, X.; Jiao, Y.; Zheng, Y.; Jaroniec, M.; Qiao, S. Z. Building up a picture of the electrocatalytic nitrogen reduction activity of transition metal single-atom catalysts. *J. Am. Chem. Soc.* **2019**, *141*, 9664–9672.
[20] Paul, S.; Sarkar, S.; Adalder, A.; Kapse, S.; Thapa, R.; Ghorai, U. K. Strengthening the metal center of Co-N_4 active sites in a 1D–2D heterostructure for nitrate and nitrogen reduction reaction to ammonia. *ACS Sustain. Chem. Eng.* **2023**, *11*, 6191–6200.
[21] Lv, X. S.; Wei, W.; Huang, B. B.; Dai, Y.; Frauenheim, T. High-throughput screening of synergistic transition metal dual-atom catalysts for efficient nitrogen fixation. *Nano Lett.* **2021**, *21*, 1871–1878.
[22] Geng, Z.; Liu, Y.; Kong, X.; Li, P.; Li, K.; Liu, Z.; Du, J.; Shu, M.; Si, R.; Zeng, J. Achieving a record-high yield rate of 120.9 $\mu g_{NH_3}\cdot mg_{cat.}^{-1}\cdot h^{-1}$ for N_2 electrochemical reduction over Ru single-atom catalysts. *Advanced Materials* **2018**, *30*, 1870301.
[23] Shi, L.; Yin, Y.; Wang, S. B.; Sun, H. Q. Rational catalyst design for N_2 reduction under ambient conditions: Strategies toward enhanced conversion efficiency. *ACS Catal.* **2020**, *10*, 6870–6899.
[24] Ghoshal, S.; Ghosh, A.; Roy, P.; Ball, B.; Pramanik, A.; Sarkar, P. Recent progress in computational design of single-atom/cluster catalysts for electrochemical and solar-driven N_2 fixation. *ACS Catal.* **2022**, *12*, 15541–15575.
[25] Zhang, L. L.; Ding, L. X.; Chen, G. F.; Yang, X. F.; Wang, H. H. Ammonia synthesis under ambient conditions: Selective electroreduction of dinitrogen to ammonia on black phosphorus nanosheets. *Angew. Chem.* **2019**, *131*, 2638–2642.
[26] Ou, P. F.; Zhou, X.; Meng, F. C.; Chen, C.; Chen, Y. Q.; Song, J. Single molybdenum center supported on N-doped black phosphorus as an efficient electrocatalyst for nitrogen fixation. *Nanoscale* **2019**, *11*, 13600–13611.
[27] Liu, K.; Fu, J. W.; Zhu, L.; Zhang, X. D.; Li, H. M.; Liu, H.; Hu, J. H.; Liu, M. Single-atom transition metals supported on black phosphorene for electrochemical nitrogen reduction. *Nanoscale* **2020**, *12*, 4903–4908.
[28] Liu, C. W.; Li, Q. Y.; Wu, C. Z.; Zhang, J.; Jin, Y. G.; MacFarlane, D. R.; Sun, C. H. Single-boron catalysts for nitrogen reduction reaction. *J. Am. Chem. Soc.* **2019**, *141*, 2884–2888.
[29] Shi, L.; Li, Q.; Ling, C. Y.; Zhang, Y. H.; Ouyang, Y. X.; Bai, X. W.; Wang, J. L. Metal-free electrocatalyst for reducing nitrogen to ammonia using a Lewis acid pair. *J. Mater. Chem. A* **2019**, *7*, 4865–4871.
[30] Kresse, G.; Joubert, D. From ultrasoft pseudopotentials to the projector augmented-wave method. *Phys. Rev. B* **1999**, *59*, 1758–1775.
[31] Kresse, G.; Furthmüller, J. Efficient iterative schemes for *ab initio* total-energy calculations using a plane-wave basis set. *Phys. Rev. B* **1996**, *54*, 11169–11186.
[32] Blöchl, P. E. Projector augmented-wave method. *Phys. Rev. B* **1994**, *50*, 17953–17979.
[33] Perdew, J. P.; Chevary, J. A.; Vosko, S. H.; Jackson, K. A.; Pederson, M. R.; Singh, D. J.; Fiolhais, C. Atoms, molecules, solids, and surfaces: Applications of the generalized gradient approximation for exchange and correlation. *Phys. Rev. B* **1992**, *46*, 6671–6687.
[34] Perdew, J. P.; Wang, Y. Accurate and simple analytic representation of the electron-gas correlation energy. *Phys. Rev. B* **1992**, *45*, 13244–13249.
[35] Monkhorst, H. J.; Pack, J. D. Special points for Brillouin-zone integrations. *Phys. Rev. B* **1976**, *13*, 5188–5192.
[36] Henkelman, G.; Arnaldsson, A.; Jónsson, H. A fast and robust algorithm for Bader decomposition of charge density. *Comput. Mater. Sci.* **2006**, *36*, 354–360.
[37] Kresse, G.; Hafner, J. *Ab initio* molecular dynamics for liquid metals. *Phys. Rev. B* **1993**, *47*, 558–561.
[38] Nosé, S. A unified formulation of the constant temperature molecular dynamics methods. *J. Chem. Phys.* **1984**, *81*, 511–519.
[39] Peterson, A. A.; Abild-Pedersen, F.; Studt, F.; Rossmeisl, J.; Nørskov, J. K. How copper catalyzes the electroreduction of carbon dioxide into hydrocarbon fuels. *Energy Environ. Sci.* **2010**, *3*, 1311–1315.
[40] Nørskov, J. K.; Rossmeisl, J.; Logadottir, A.; Lindqvist, L.; Kitchin, J. R.; Bligaard, T.; Jønsson, H. Origin of the overpotential for oxygen reduction at a fuel-cell cathode. *J. Phys. Chem. B* **2004**, *108*, 17886–17892.
[41] Umer, M.; Umer, S.; Zafari, M.; Ha, M. R.; Anand, R.; Hajibabaei, A.; Abbas, A.; Lee, G.; Kim, K. S. Machine learning assisted high-throughput screening of transition metal single atom based superb hydrogen evolution electrocatalysts. *J. Mater. Chem. A* **2022**, *10*, 6679–6689.
[42] Boonpalit, K.; Wongnongwa, Y.; Prommin, C.; Nutanong, S.; Namuangruk, S. Data-driven discovery of graphene-based dual-atom catalysts for hydrogen evolution reaction with graph neural network and DFT calculations. *ACS Appl. Mater. Interfaces* **2023**, *15*, 12936–12945.
[43] Greeley, J.; Nørskov, J. K. Electrochemical dissolution of surface

alloys in acids: Thermodynamic trends from first-principles calculations. *Electrochim. Acta* **2007**, *52*, 5829–5836.

[44] Guo, X. Y.; Gu, J. X.; Lin, S. R.; Zhang, S. L.; Chen, Z. F.; Huang, S. P. Tackling the activity and selectivity challenges of electrocatalysts toward the nitrogen reduction reaction via atomically dispersed biatom catalysts. *J. Am. Chem. Soc.* **2020**, *142*, 5709–5721.

[45] Guo, X. Y.; Lin, S. R.; Gu, J. X.; Zhang, S. L.; Chen, Z. F.; Huang, S. P. Simultaneously achieving high activity and selectivity toward two-electron O_2 electroreduction: The power of single-atom catalysts. *ACS Catal.* **2019**, *9*, 11042–11054.

[46] Ling, C. Y.; Ouyang, Y. X.; Li, Q.; Bai, X. W.; Mao, X.; Du, A. J.; Wang, J. L. A general two-step strategy-based high-throughput screening of single atom catalysts for nitrogen fixation. *Small Methods* **2019**, *3*, 1800376.

[47] Ma, L. H.; Xu, F. F.; Zhang, L. L.; Nie, Z. F.; Xia, K.; Guo, M. X.; Li, M. Z.; Ding, X. Breaking the linear correlations for enhanced electrochemical nitrogen reduction by carbon-encapsulated mixed-valence $Fe_7(PO_4)_6$. *J. Energy Chem.* **2022**, *71*, 182–187.

[48] Skúlason, E.; Bligaard, T.; Gudmundsdóttir, S.; Studt, F.; Rossmeisl, J.; Abild-Pedersen, F.; Vegge, T.; Jónsson, H.; Nørskov, J. K. A theoretical evaluation of possible transition metal electro-catalysts for N_2 reduction. *Phys. Chem. Chem. Phys.* **2012**, *14*, 1235–1245.

[49] Chen, Z. Z.; Zhang, X.; Lu, G. Overpotential for CO_2 electroreduction lowered on strained penta-twinned Cu nanowires. *Chem. Sci.* **2015**, *6*, 6829–6835.